PAPER

Check for updates

Size-dependent catalytic activity for CO oxidation over sub-nano-Au clusters†

Yuqi Wang,[a] Haoxiang Xu,*[a] Jiqin Zhu*[b] and Daojian Cheng 🆔 *[a]

Gold (Au) nanocatalysts present outstanding activity for many reactions and have long attracted much attention, but the size effect of sub-nano-clusters on catalytic activity lacks systematic research. Using CO oxidation as a probe reaction, the size-dependent catalytic capability of sub-nano-Au clusters was explored. The global-minimum (GM) structures of Au_N (N = 2–300, <2.5 nm) were obtained utilizing revised particle swarm optimization (RPSO) combined with density functional theory (DFT) calculations and the Gupta empirical potential. Geometric structural descriptors built a bridge among geometric features, adsorption energy, and the CO oxidation rate of each site of any given sub-nano-Au clusters, making it possible for high-throughput evaluation of the adsorption energy and catalytic activity of the whole sub-nano-Au cluster. The activity per unit mass of sub-nano-Au clusters shows a volcano-shaped relationship with the cluster size, where the sub-nano-Au clusters with a 0.75 nm diameter possess the highest CO_2 formation rate per unit mass. The *Edge* and *Kink* sites have a higher turnover frequency (approximately 10^6) than the *Face* sites (approximately 10^2), which contribute the most to CO_2 formation. The weak adsorption of CO and O_2 was found to be a crucial factor determining the inferior activity of the *Face* site to the *Kink* and *Edge* sites. The adsorption process rather than the surface reaction step becomes the rate-determining step on the *Face* site, attributed to the decreased activity per unit mass of sub-nano-Au clusters. This work provides an in-depth mechanistic understanding of size-dependent catalytic activity for Au clusters at the sub-nano level.

1 Introduction

Gold (Au) had been considered chemically inert for a long time, until the discovery of Au clusters' remarkable catalytic properties by Hutchings *et al.* in their pioneering works.[1] Au clusters have exhibited extraordinarily high activities for various reactions,[2] including low-temperature catalytic combustion, partial oxidation of hydrocarbons, selective reduction of nitrogen oxides,[3] *etc.* The high activity of these Au clusters could be partly attributed to their high surface-to-volume ratio, surface atom arrangement, low-coordinated atoms and so on.[4] On the one hand, the constituent atoms of the Au clusters are arranged in a significantly different manner from that of bulk gold to reduce the surface energy.

On the other hand, the electronic structures of Au clusters are quantized with an energy gap so that reactants can be activated *via* electron transfer.[5]

Donoeva *et al.*,[2] Sh. K. Shaikhutdinov *et al.*,[6] and G. R. Bamwenda *et al.*[7] explored the CO catalytic activity of Au clusters at the nanoscale (at least 2.5 nm). In this range, only Au particles smaller than 5 nm are active in low-temperature CO oxidation,[2] and a further increase in the cluster diameter above 3 nm leads to a decrease in the activity of Au clusters.[7] Celine *et al.* for the first time reported the experimental evidence that nano-Au island films have the same CO adsorption behavior as both large Au particles and extended Au surfaces,[8] which highlights the particularity of sub-nano-Au clusters. For sub-nano-structures, the ultra-small size induces strong electron energy quantization.[4] Yamazoe *et al.* discovered that sub-nano-Au clusters less than 2 nm could show obvious catalytic effects in various aerobic oxidation reactions. In the hydrogenation processes, gold nanoparticles ranging from 1 to 2 nm exhibit good catalytic activity.[9]

The outstanding catalytic properties of Au clusters are highly dependent on their size.[10,11] Size effects on adsorption and reactivity play a very important role in the excellent catalytic performance of Au clusters, a phenomenon that has

[a] State Key Laboratory of Organic–Inorganic Composites, Beijing Key Laboratory of Energy Environmental Catalysis, Beijing University of Chemical Technology, Beijing 100029, People's Republic of China. E-mail: xuhx@buct.edu.cn, chengdj@mail.buct.edu.cn

[b] State Key Laboratory of Chemical Resource Engineering, Beijing University of Chemical Technology, Beijing 100029, People's Republic of China. E-mail: zhujq@mail.buct.edu.cn

†Electronic supplementary information (ESI) available. See DOI: https://doi.org/10.1039/d4nr02705a

been observed for decades.[8] Goodman's group invoked the concept of quantum effects.[3] The size-dependent catalytic activity could be attributed to the size-dependent adsorption behaviors, which are induced by the size-dependent electronic structures of Au clusters.[12]

The exploration of size-dependent catalytic activity through theoretical calculations has also been conducted. Nørskov *et al.* predicted that Au_{10} can be highly active for CO oxidation in the gas phase.[13] Bernhardt *et al.* revealed the full reaction cycle of CO oxidation on Au_2 and Au_3 by performing *ab initio* calculations.[14,15] Kaatz *et al.* studied larger Au clusters (2–6 nm) to conclude that low coordination leads to a higher turnover frequency.[16] However, the size-dependent catalytic activity in lots of literature is limited to the nanoscale (>3 nm), and the Au cluster models are often established through highly symmetric polyhedral configurations or employing Wulff construction rules, which retain the atom arrangement of the Au bulk crystal structure. As for sub-nano-Au clusters (<3 nm) with GM structures tend to be irregular, neither the distribution of active sites nor size-dependent catalytic activity has long been a lack of attention, which hinders the construction of sub-nano-Au clusters with enhanced catalytic performance. The lack of both sub-nano-Au clusters' GM configuration and detailed structure–activity research within this diameter range is not conducive to further progress of Au catalysts.

In this paper, using CO oxidation as a probe reaction, a comprehensive study of Au clusters at the sub-nano level was carried out, mainly focusing on Au clusters composed of 2 to 300 atoms with a diameter less than 2.5 nm. Their GM configurations were identified using the RPSO algorithm based on DFT calculations and the Gupta empirical potential. The elaborate description of size-dependent catalytic performance at each site one by one was achieved by the systematic classification of adsorption sites utilizing the generalized coordination number. A geometry–adsorption–activity relationship is built to analyze the size-dependent catalytic activity of sub-nano-Au clusters. Aided by a microkinetic model and electronic structure analysis, a detailed discussion of how the geometric coordination feature of reaction sites affects catalytic performance was conducted.

2 Computational details

2.1 Revised particle swarm optimization

Based on the particle swarm algorithm (PSO), which is an efficient method for global optimization, our group developed a revised particle swarm optimization (RPSO) algorithm in order to overcome the tendency of the original PSO to be easily trapped in local minima.[17] RPSO consists of a random learning procedure, competition strategy, confusion policy, and mutation mechanism. These efforts make RPSO an outstanding algorithm for the global optimization of complex nonlinear systems. In the previous work,[17] the global optim-

ization of Lennard-Jones (LJ), elemental metal, and bimetallic clusters was conducted successfully, which strongly supports the efficiency. The evolution part of the RPSO could be explained by the following equation:

$$V_i^{k+1} = \omega V_i^k + c_1 r_1 (P_i^k - X_i^k) + c_2 r_2 (P_g^k - X_i^k) + c_3 r_3 (P_r^k - X_i^k) \tag{1}$$

where V_i^k is the velocity of the particle i in the swarm at iteration k. ω remains the same as the original PSO standing for the inertia weight factor from 0.9 to 1. Besides c_1 and c_2 as acceleration constants, RPSO imports a new acceleration constant c_3 to maintain population diversity. r, r_2, and r_3 are uniformly distributed random numbers between 0 and 1. The four parts on the right side of eqn (1) are named inertia, local, global, and random. The term random represents the random learning procedure that could boost the convergence speed.

2.2 Structural global optimization of Au clusters

The potential energy surface (PES) of Au clusters is explored using RPSO combined with first-principles calculations as well as the Gupta empirical potential. The RPSO method is capable of surmounting the high barrier on the PES and identifying GM structures. The capability of this method for exploring the PES has been demonstrated for both transition monometallic clusters like Ag^{18} and bimetallic Pt–Pd clusters.[17] The Rosenbrock function of different dimensions[17,19] and 15 benchmark functions in CEC[17,20] served as test cases, and RPSO showed better performance in searching for the global best solution. Although RPSO is a global optimization method with high efficiency, its application with DFT calculations is still time-consuming. Therefore, Au clusters with more than 20 atoms are searched with RPSO at the Gupta empirical potential level to make a trade-off between precision and efficiency in this work. The empirical potential is much more efficient in generating highly symmetric Au structures with lower computational costs than *ab initio* methods.[21,22] The Gupta potential in this work could enable a reasonable description of the metal clusters' PES.[23] Additionally, empirical potentials originate from the approximation of bulk materials and thus are prone to overestimating atomic interactions, which can affect the evaluation of system energy. Therefore, an energy correction step is necessary.
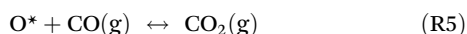
All calculations of freestanding Au clusters are carried out with a vacuum layer of at least 10 Å in all three directions to prevent interaction forces from influencing the results. All DFT calculations are performed using the VASP package.[24] For the calculation of electronic energies, a kinetic energy cutoff of 400 eV and an electronic self-consistency criterion of 10^{-5} eV are used. In the application of the Gupta potential, the parameters of Au are listed in Table S1.†

2.3 Recognition of surface sites of sub-nano-Au clusters

Due to the complexity of the three-dimensional surfaces of clusters, previous theoretical exploration of catalytic reactions upon surfaces mainly focused on regular shaped surfaces or a few specific adsorption sites. In this paper, we employed the alpha shape algorithm, which traverses the atom set to construct triangulation sequentially, and the key parameter α is determined based on the radius of the outer sphere of the obtained spatial tetrahedron. The value of α regulates the shape of the concave package. A larger α corresponds to a rougher enclosure, and as α approaches infinity, the concave enclosure degenerates into a convex. Therefore, the binary search method can be used to determine the appropriate α value to suit different systems. This tactic could facilitate the identification and further exploration of all surface sites of large-scale complex structures. The ideal minimum concave is a polyhedral cover of a known atom set, which is also called an alpha shape (Fig. S1† shows an example). There have been mature implementations of finding alpha shapes and the open-source Python package Alphashape 1.3.1 was chosen in this work.[25] Based on this method, all surface atoms that have the potential to participate in reactions could be identified successfully.

2.4 Microkinetic model of CO oxidation

CO oxidation was modeled with the L–H mechanism. The whole reaction could be divided into five steps, namely co-adsorption of CO and O_2 ((R1) and (R2)), formation of OOCO intermediates (R3), dissociation of OOCO intermediates into CO_2 and atomic oxygen (R4), and the reaction of the second CO molecule with the remaining adsorbed oxygen atoms to produce the second carbon dioxide molecule (R5).

$$CO(g) + * \leftrightarrow CO* \tag{R1}$$

$$O_2(g) + * \leftrightarrow O_2* \tag{R2}$$

$$CO* + O_2* \leftrightarrow OOCO* \tag{R3}$$

$$OOCO* \leftrightarrow CO_2(g) + O* \tag{R4}$$

$$O* + CO(g) \leftrightarrow CO_2(g) \tag{R5}$$

The asterisk (*) indicates the adsorbed species. The experimental conditions for the CO oxidation reaction are as follows: the temperature denoted as T is 298 K, the partial pressure of CO is 0.01 bar, and the partial pressure of O_2 is 0.21 bar. In the following equations, k represents Boltzmann's constant, and h represents Planck's constant. In (R1) and (R2), their reaction equilibrium constants are denoted as K_1 and K_2, respectively. $\Delta E_1 = E_{ad}(CO)$ stands for CO adsorption energy. $\Delta E_2 = E_{ad}(O_2)$ stands for O_2 adsorption energy. ΔS_1 and ΔS_2 represent the change of entropy in the adsorption process of the corresponding gas molecules. $\Delta S_1 = -197.71$ J mol^{-1} K^{-1} and $\Delta S_2 = -205.1$ J mol^{-1} K^{-1}.

$$K_1 = \exp\left(\frac{-(\Delta E_1 - T\Delta S_1)}{kT}\right) \tag{2}$$

$$K_2 = \exp\left(\frac{-(\Delta E_2 - T\Delta S_2)}{kT}\right) \tag{3}$$

In reaction (R3), the adsorbed CO and O_2 are close to each other and then overcome the first activation energy barrier (E_{a1}), reach the transition state 1 (TS$_1$) and form the intermediate complex OOCO*. k_3^+ represents the forward reaction rate constant and k_3^- represents the reverse reaction rate constant. Assuming that the entropy of the adsorbate is zero, it follows that $\Delta S_3 = 0$. E_{a3}^+ represents the forward reaction activation energy barrier, E_{a3}^- represents the reverse reaction activation energy barrier, E_{co-ad} means the co-adsorption energy of the oxygen molecule and carbon monoxide, E_{TS-1} means the first transition state energy of the elementary reaction (R3), and E_{OOCO} means the relative energies of intermediate states OOCO.

$$k_3^+ = \frac{kT}{h} \exp\left(\frac{-(E_{a3}^+ - T\Delta S_3^+)}{kT}\right) \tag{4}$$

$$k_3^- = \frac{kT}{h} \exp\left(\frac{-(E_{a3}^- - T\Delta S_3^-)}{kT}\right) \tag{5}$$

$$E_{a3}^+ = E_{TS-1} - E_{co-ad} \tag{6}$$

$$E_{a3}^- = E_{TS-1} - E_{OOCO} \tag{7}$$

In reaction (R4), the unstable peroxide OOCO* intermediate is dissociated and overcomes the activation energy (E_{a2}) to reach the transition state 2 (TS$_2$), resulting in a CO_2 molecule and an adsorbed oxygen atom. k_4 means the forward reaction rate constant. The same assumption implies that the entropy of adsorption is zero, so ΔS_4 is still zero. E_{a4} stands for the activation energy barrier. E_{TS-2} means the second transition state energy of the elementary reaction (R4).

$$k_4 = k_4^+ = \frac{kT}{h} \exp\left(\frac{-(E_{a4} - T\Delta S_4^+)}{kT}\right) \tag{8}$$

$$E_{a4} = E_{TS-2} - E_{OOCO} \tag{9}$$

In reaction (R5), the adsorbed oxygen atom directly interacts with another CO molecule to form a second CO_2. Since (R5) usually exhibits a very low activation energy barrier,[26,27] this last reaction is not the rate-controlling step. The expression formula of OOCO coverage can be obtained by ignoring the weak influence of the non-speed control step (R5). The coverage of OOCO satisfies the following equation:

$$\theta_{OOCO} = \frac{k_3^+}{k_3^- + k_4^+} \theta_{CO} \theta_{O_2} \tag{10}$$

Given that the barrier of reaction (R5) is negligible, the coverage of the O atom is set to 0. Here in the microkinetic model of CO oxidation on Au clusters based on the L–H mechanism, the sum of all intermediates and free top adsorption sites is equal to 1.

$$\theta_* + \theta_{CO} + \theta_{O2} + \theta_{OOCO} = 1 \tag{11}$$

Based on the derivation of the above formulas, it can be obtained that the coverage rate of free adsorption sites satisfies the following equation:

$$\theta_* = \frac{1}{1 + K_1 p(CO) + K_2 p(O_2) + \frac{k_3^+}{k_3^- + k_4^+} K_1 K_2 p(CO) p(O_2) \theta_*}$$ (12)

Finally, as the goal of the final kinetic analysis, the CO_2 conversion rate is determined using the following formula:

$$\text{Rate} = \text{rate}(R4) = k_4^+ \theta_{OOCO}$$ (13)

Through the analysis of the above series of mathematical relations, six parameters affecting the oxidation rate of CO were obtained: $E_{ad}(CO)$, $E_{ad}(O_2)$, E_{TS-1}, E_{TS-2}, E_{co-ad}, and E_{OOC}. The first two parameters could be obtained through the geometry–adsorption relationship in the Results and discussion section. The last four parameters could be calculated through the following equations:

$$E_{co-ad} = 1.51 \times [E_{ad}(O_2) + E_{ad}(CO)] + 0.08$$ (14)

$$E_{TS-1} = 0.75 \times E_{co-ad} - 0.12$$ (15)

$$E_{OOCO} = 1.49 \times E_{co-ad} + 0.85$$ (16)

$$E_{TS-2} = 0.71 \times E_{OOCO} - 0.16$$ (17)

3.   Results and discussion

3.1   Structural global optimization of sub-nano-Au clusters

As shown in Fig. 1 and Fig. S2(a–c),† RPSO could filter out the global optimal structure of clusters. The bonding information and cluster diameter are shown in Fig. S3 and S4.† The analysis of energy is as follows. The cohesive energies for finite cluster sizes are defined as

$$E_{coh} = (NE_{Au} - E_{cluster})/N$$ (18)

where E_{Au} denotes the electronic energy of the free Au atom and $E_{cluster}$ denotes the total energy of the Au$_N$ cluster with N atoms. The calculated results of cohesive energy are well consistent with the previous work[23,28] (see Table S2†). Most of the structures are consistent with the literature. Some biased structures, such as Au$_{20}$, are different from their GM structures, but with only a small difference in energy. The disparity between the extrapolation intercept and bulk cohesive energy in Fig. 2(a) exposes a universal problem that DFT methods fail to accurately describe strongly correlated systems like Au bulk[23] (also shown in Fig. S6†). Meanwhile, different DFT functionals characterize the binding situation differently and hence result in substantially different cohesive energies.[28,29] Because the parameters used in the empirical potential were obtained by fitting the bulk properties,[30] it is reasonable that the Gupta potential could properly reflect the tendency of larger systems but fail to describe the interactions among Au atoms in sub-nano-clusters, as shown in Fig. S5.† This also indicates the
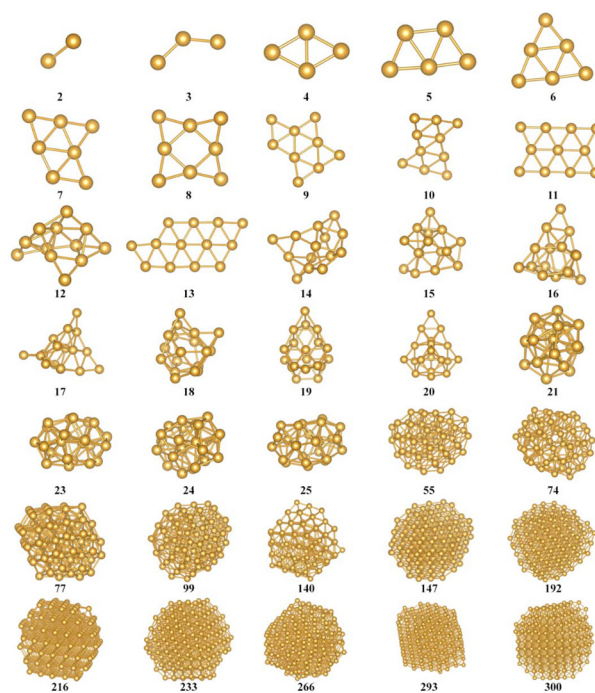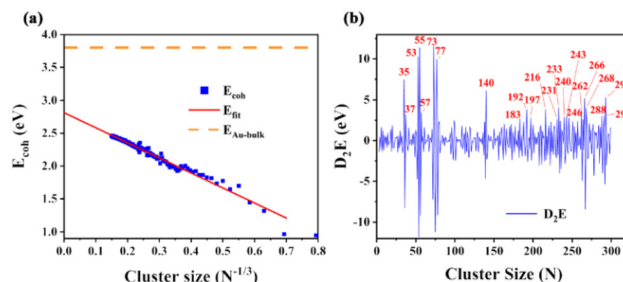

Fig. 1 Snapshots of some sub-nano-Au$_N$ clusters' (N = 2–300) GM structures obtained by RPSO. Au$_N$ (N = 2–20) structures are determined by RPSO at the DFT level. Au$_N$ (N = 21–300) structures are found by RPSO at the Gupta level. Other structures are shown in Fig. S2(a–c).† All coordinate files are provided in the ESI.†

Fig. 2 (a) The calculated cohesive energy of Au$_N$ (N = 2–300) related to cluster size. The red line denotes extrapolation from N = 3–300. The orange dashed line indicates the observed cohesive energy of bulk gold, which is 3.8 eV.[23] (b) D$_2$E (second finite difference) of Au$_N$ (N = 2–300). Red label numbers correspond to sizes with significantly high values.

necessity of DFT corrective measures to structures at the Gupta level. Considering the common defects of nanostructures described by empirical potentials, the corrective measure is conducted when dealing with clusters optimized at the Gupta level, as shown in Fig. S5.† In the range of 21–300, some of the Au$_N$ structures were selected to perform self-consistent field DFT calculations. There is always a linear relationship between the total energy of the system and the number of atoms; thus using the selected data points to correct the whole line of original energy at the Gupta level is possible.

For GM structures screened by RPSO, a quantity to assess their cluster stability is the second finite difference (D_2E). D_2E could depict clusters' stability relative to their $N+1$ and $N-1$ neighbors. It is calculated as follows:

$$D_2E = E_{N+1} + E_{N-1} - 2E_N \quad (19)$$

E_N corresponds to the calculated total energy of Au_N consisting of N atoms. Clusters with larger D_2E have higher stability than their neighbors in Fig. 2(b). Those remarkably stable Au_N clusters are consistent with previous works.[31,32] It has been reported that these clusters at the pure DFT level are relatively stable ($N = 4, 6, 8, 10, 12, 14,$ and 18),[33,34] and the results in Fig. S7† are in good agreement with these findings, indicating the reliability of RPSO.

3.2 Geometry–adsorption relationship

The generalized coordination number (CN_g) and relative curvature angle (CA_r) serve as efficient geometric descriptors for the adsorption energy of CO/O_2 on Au clusters. These two geometric descriptors are the basis of the geometry–adsorption correlation model in this paper.

The coordination number (CN) is used as an index to describe the coordination saturation of an atom. As shown in Fig. 3(a), the atom q is five-coordinated. The atom in bulk Au has the largest coordination number, with a single atom surrounded by its 12 closest neighbors. Au atoms with coordination numbers below 12 tend to form bonds to compensate for reduced coordination. Based on the definition of the tra-

ditional coordination number, the generalized coordination number (CN_g) is adopted in this work to describe the trend of adsorption strength on Au clusters' surface more precisely. The CN_g of the atom p is calculated using the weighted sum of traditional coordination numbers of all the first nearest neighbor atoms through the following equation and also shown in Fig. 3(b):

$$CN_g^p = \frac{\sum\limits_q CN^q}{CN_{max}} \quad (20)$$

CN_{max} of 12 corresponds to the maximum coordination number achieved by a face-centered cubic Au structure. CN^q represents the coordination number of the atom q, which comes from a collection of all nearest neighbors of the atom p. The bonding threshold of Au clusters is set to 3.3 Å, which is used to determine the bonding information of atoms.

The relative curvature angle of the atom p (CA_r^p) is defined as follows. The first thing to do is to obtain the collection S consisting of all nearest neighbors of the atom p. The next step is to deal with the different cases of the set S. (1) When the number of elements in the set S does not exceed 1, then the curvature angle CA^p is defined as 0. (2) When the number of elements in the set S is exactly equal to 2, the curvature angle CA^p is defined as θ in Fig. 3(c). (3) The set S has more than 3 elements. As shown in Fig. 3(d), the curvature angle is calculated by averaging the sum of all θ'. Any atom q (q is the atom with the closest Euclidean distance to the atom p from the collection S) is randomly chosen. The straight line between the atom p and the atom q is denoted as the line pq. Any atom r in S except q is selected and then the atom s nearest to r except the atom q in S is selected, and these two atoms form a line sr. The imaginary point t is the midpoint of the line rs. The line between the atom p and point t is denoted as the line tp. θ' is determined by the line pq and line tp. The atom q may have more than one choice (some atoms in S have the same distance as the target atom p), but after random selection, there would be only one certain atom selected. The atom q has at least two choices (the collection S has more than 3 members); meanwhile, the atom r and atom s have more combinations. Each of these different combinations will yield a value of θ'. After going through all these combinations, the average result of all θ' is the curvature angle of the atom p, namely CA^p. After discussing the above three cases, the curvature angle CA^p of the atom p will be obtained. Finally, the relative curvature angle of the atom p (CA_r^p) is then simply normalized using 180 degrees, as shown in the following equation:
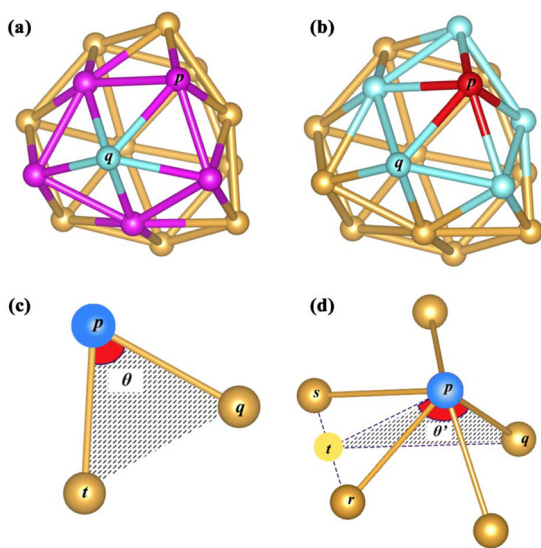
$$CA_r^p = \frac{CA^p}{180} \quad (21)$$

Fig. 3 (a) Coordination number of the blue atom q, which equals the number of pink atoms p. (b) The CN_g of the red atom p is calculated according to the weighted average of the coordination numbers of blue atoms q. (c) The CA_r of the blue atom p is denoted as θ when there are two nearest neighbors around p. (d) If the atom p has more than three atoms in the set of nearest neighbors, CA_r is calculated according to the weighted average of θ'. Imaginary point t is located at the midpoint between the atom s and atom r. All displayed Au atoms are nearest neighbors of the blue atom p.

Based on previously defined geometric descriptors, the adsorption energies of CO and O_2 on the top sites of freestanding sub-nano-Au clusters could be depicted systematically. Adsorption energies are defined as $E_{ads} = E_{adsorbate+cluster} - E_{adsorbate} - E_{cluster}$. As shown in Fig. 4, there are linear relationships[35,36] between geometric descriptors and adsorp-
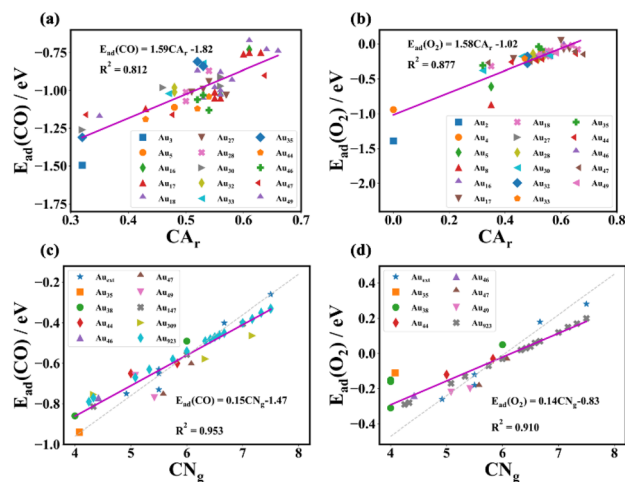
Fig. 4 All data on adsorption energy are cited from ref. 27, 28 and 37–44. (a) The linear relationship between CO adsorption energies and CA_r. (b) The linear relationship between O_2 adsorption energies and CA_r. (c) The linear relationship between CO adsorption energies and CN_g. Au_{ext} represents the adsorption data of extended gold surfaces, including Au(100), Au(111), Au(110), Au(211), Au(321), and Au(553). The gray dashed line represents the trend of crystal surface adsorption energy, which is $E_{ad}(CO) = 0.2 \times CN_g - 1.76$. (d) The linear relationship between O_2 adsorption energies and CN_g. The meaning of Au_{ext} and the gray dashed line remains the same as before. The crystal surface adsorption energy follows $E_{ad}(O_2) = 0.23 \times CN_g - 1.39$.

tion energies. The data points in Fig. 4 were obtained from ref. 27, 28 and 37–44. It is credible that such an adsorption energy linear relationship has a certain universality based on lots of data coming from multiple references.

When $CN_g < 4$, CA_r is chosen to quantify the geometry effect on adsorption energies, as shown in Fig. 4(a) and (b). For atoms with $CN_g > 4$, it is possible to deal with predicting adsorption energy using CN_g. These linear relationships could serve as reliable and useful tools for evaluating trends in adsorption energy, as stated in Nørskov's previous research that lines are much more precise than points.[45] All linear relationships were obtained by least squares fits using the Python package Numpy.[46] As a result, the adsorption energies could be correlated with geometric descriptors *via* the following equations:

$$E_{ad}(CO) = 1.59CA_r - 1.82 \ (CN_g < 4) \tag{22}$$

$$E_{ad}(O_2) = 1.58CA_r - 1.02 \ (CN_g < 4) \tag{23}$$

$$E_{ad}(CO) = 0.15CN_g - 1.47 \ (CN_g \geq 4) \tag{24}$$

$$E_{ad}(O_2) = 0.14CN_g - 0.83 \ (CN_g \geq 4) \tag{25}$$

3.3 Size-dependent adsorption properties of sub-nano-Au clusters

When exploring the adsorption properties of clusters, the first thing to do is to determine which atoms could act as adsorbed sites. Because of the complexity of the surface environment of

irregular sub-nano-clusters, it is almost impossible to manually find a large number of exposed surface atoms in a large set of complex structures. Top sites are taken into consideration for some simplification. Thus, each top site on the outer surface would be recognized, which provides a reasonable criterion for measuring catalytic activity.

According to the linear relationship in Fig. 4, the CO and O_2 adsorption energies of all studied sub-nano-Au_N clusters ($N = 2$–300) can be evaluated. As shown in Fig. 5(a), with increasing cluster size, the adsorption energy of CO adsorbed on sub-nano-Au_N clusters gradually approaches that of extended Au surfaces, namely Au(211), Au(100) and Au(111). It indicates that the atomic arrangement of surface sites of sub-nano-Au_N clusters gradually achieves greater coordination saturation accompanied by a larger cluster size. The gradual increase in the coordination saturation of surface atoms leads to the adsorption behavior of sub-nano-Au_N clusters approaching those of Au(211), Au(100), and Au(111) in sequence. It is the similarity of the local coordination environment that results in similar CO adsorption performance.

A similar size-dependent adsorption trend also occurs when observing adsorbed O_2 in Fig. 5(b). Since the atomic coordination environment on the surface of a given structure does not change, the corresponding relative relationship of adsorption energy is the same, which follows the law that the adsorption of the corresponding gas molecules becomes weaker with the increase of cluster size. Different from CO adsorption, the adsorption of molecular oxygen on extended crystal surfaces with high CN_g (Au(111) and Au(100)) is much
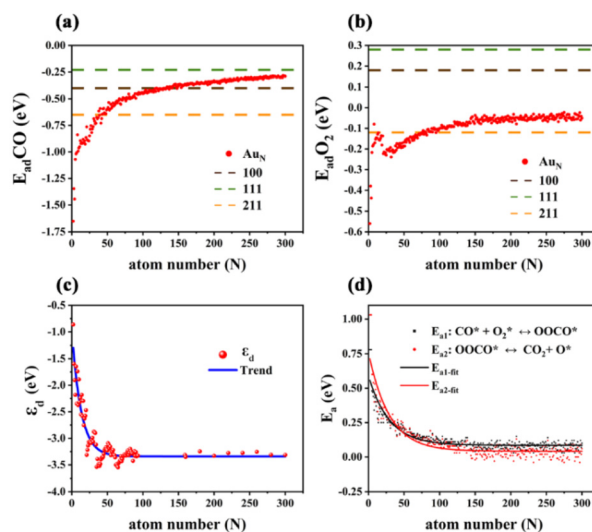

Fig. 5 (a) The average adsorption energy of CO upon sub-nano-Au clusters. Dashed lines represent adsorption energy on the corresponding Au crystal faces respectively, cited from ref. 23 and 43. (b) The average adsorption energy of molecular O_2 upon sub-nano-Au clusters. Dashed lines represent adsorption energy on the corresponding gold crystal face respectively, cited from ref. 27. (c) The d-band center (ε_d) of sub-nano-Au clusters. (d) The energy barrier of the elementary steps of CO oxidation as a function of the size of sub-nano-Au clusters.

weaker than that of CO. As shown in Fig. 4(c and d), gray dashed lines represent the trend of adsorption energy on the crystal surface. The fitted lines of CO adsorption energy between clusters and crystal surfaces are closer, while there is a significant difference in the trend lines of O_2 adsorption energy. Therefore, as the cluster size increases, the CO adsorption energy of clusters approaches the value of crystal surfaces, while the O_2 adsorption energy deviates from that. The stronger reactant adsorption of sub-nano-Au clusters can to some extent explain their better catalytic activity compared to bulk gold. Adsorption as a function of the cluster diameter follows a linear logarithmic trend as shown in Fig. S8.†

For post-transition metals like Au, the lower the d band center, the weaker the adsorption strength.[47,48] As the cluster size increases, the surface atoms become more tightly arranged and the coordination number is generally higher, resulting in enhanced d orbital interactions of gold atoms. The enhanced interaction of the orbitals is accompanied by the d orbitals occupying a wider energy range, namely a wider d bandwidth. Therefore, a lower d band center would appear in Fig. 5(c) and that is the reason why size-dependent adsorption behaves as scatters in Fig. 5(a) and (b). Naturally, when the cluster size increases to a certain extent, there is little room for the atoms to get more compact so the d band center no longer decreases continuously and fluctuates only in a very small range.

3.4 Size effect of sub-nano-Au clusters on CO oxidation reaction kinetics

According to the microkinetic analysis in section 2.4, (R3) and (R4) play the role of a rate controller. Their energy barriers are all plotted in Fig. 5(d). E_{a1} is the energy barrier for (R3) and E_{a2} is the energy barrier for (R4). Both of them conform to a single exponential decay distribution as follows. E_{a1} yields an R^2 value of 0.854 and E_{a2} yields an R^2 value of 0.856.

$$E_{a1} = 0.5052 \times \exp(-N/29.1161) + 0.0852 \quad (26)$$

$$E_{a2} = 0.7188 \times \exp(-N/29.1768) + 0.0419 \quad (27)$$

On the basis of the L–H mechanism, the reaction energy barrier of the reaction pathway has not exceeded 0.5 eV (0.5 eV energy barrier is the upper limit for a facile reaction at room temperature), which verifies the hypothesis of dominating the L–H reaction mechanism. As the cluster size increases, the reaction energy barrier continuously decreases, suggesting that elementary reaction steps on the catalyst surface become facile and may not be rate-determining steps for sub-nano-Au clusters with increasing size.

Through the application of the newly established geometry–adsorption relationships, as well as the adsorption-barrier equations above, it is possible to predict the reaction rate of CO oxidation on different surface sites of sub-nano-Au clusters. In the rate-mapping color model in Fig. 6, it is clear that clusters with different sizes have distinct distributions of active sites. The maximum and minimum values of the reaction rate are decided based on the rate data set from Au_N
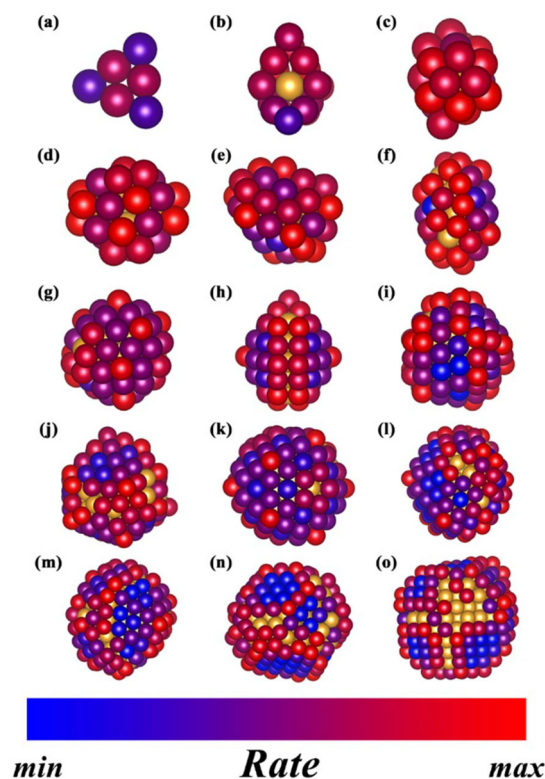

Fig. 6 Schematics of the reaction rate of CO oxidation on all surface sites of sub-nano-Au clusters, including (a) Au_6, (b) Au_{19}, (c) Au_{25}, (d) Au_{35}, (e) Au_{53}, (f) Au_{55}, (g) Au_{73}, (h) Au_{77}, (i) Au_{112}, (j) Au_{140}, (k) Au_{159}, (l) Au_{199}, (m) Au_{234}, (n) Au_{293} and (o) Au_{300}.

(2–300). Those atoms with the original golden color are inside the concave polyhedron of sub-nano-Au clusters, which are determined through the alpha shape algorithm.

In Fig. 7, the activity (CO_2 formation rate) per unit mass (APUM) is defined as follows:

$$\text{Activity per unit mass} = \frac{N_A \times \text{Rate}_{\text{tot}}}{N \times \text{AW}_{\text{Au}}} \, (s^{-1} \, g^{-1}) \quad (28)$$

where AW_{Au} = 196.967 g mol^{-1}, N_A is Avogadro's constant and Rate_{tot} is calculated from the sum of CO_2 formation rates from all surface sites on one Au_N (N = 2–300). The activity per unit mass could reflect the catalytic capacity in the CO oxidation reaction of certain sub-nano-Au clusters in Fig. 7(a and b). The correlation between the APUM and the diameter of sub-nano-Au clusters is quantitatively investigated through log–normal distribution modeling with R^2 = 0.924 as follows:

$$\text{APUM} = 0.552 + \frac{1.096}{\sqrt{2\pi} \times 0.455 \times \text{dia}} \times \exp\left[-\frac{\left(\ln\frac{\text{dia}}{0.968}\right)^2}{2 \times 0.455^2}\right]$$
$$(29)$$

The APUM trend as a function of particle diameter shows a volcano-shaped relationship, and it provides a reference for estimating the approximate optimal range of diameters for
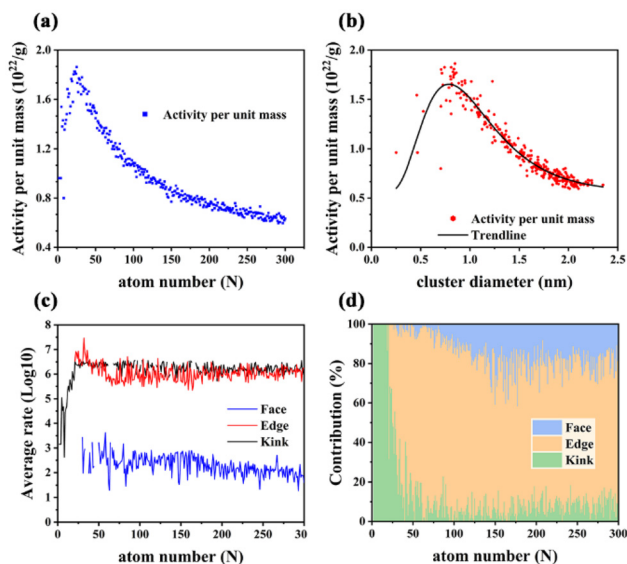
Fig. 7 (a) Size-dependent activity (CO oxidation reaction rate) per unit mass of sub-nano-Au clusters, as a function of the number of Au atoms. (b) Size-dependent activity (CO oxidation reaction rate) per unit mass of sub-nano-Au clusters, as a function of the diameter of sub-nano-Au clusters. (c) Average CO oxidation rate at different surface sites (*Kink*, *Edge*, and *Face*) of sub-nano-Au clusters as a function of the number of Au atoms. (d) Contribution from *Kink*, *Edge* and *Face* sites to the overall CO oxidation reaction rate of sub-nano-Au clusters, as a function of the number of Au atoms.

sub-nano-Au clusters. Extreme values appear when the cluster size is in the range from 21 to 30 atoms. Among them, Au_{25} displays the best catalytic performance. When the size surpasses 50 atoms, the APUM decreases as the cluster size increases. This result is consistent with the conventional view regarding the size–activity relationship of sub-nano-Au catalysts,[2,6,44] further validating the underlying size-dependent catalytic performance of sub-nano-Au clusters.

As shown in Fig. S9,† the surface sites of sub-nano-Au clusters can be classified into three kinds according to their CN_g, where *Kink* sites show the lowest CN_g smaller than 4, *Face* sites have the highest CN_g ranging from 6 to 8 and *Edge* sites correspond to medium CN_g ranging from 4 to 6. Fig. S10† shows that the proportion of surface sites would decrease as the cluster size increases. Meanwhile, the ratio of active sites (*Kink* and *Edge*) among surface sites also does not increase, as shown in Fig. S11.† Before 0.75 nm (or 25 atoms), as shown in Fig. 7c, the average rate on *Kink* sites becomes larger, and at 0.75 nm (or 25 atoms), *Edge* sites with the highest average rate begin to take part in the reaction, which leads to the maximum APUM for sub-nano-Au clusters at around 0.75 nm (or 25 atoms). As shown in Fig. S10,† the proportion of surface sites participating in the reaction decreases as their size increases. Only very small sub-nano-Au clusters could form planar structures and these 2-dimensional (D) clusters' size cannot exceed 13 atoms.[30] As long as the size of clusters becomes larger, it is almost certain to get 3-D GM structures. Therefore, Au clusters with a size over 50 atoms would exhibit

3D polyhedral structures. For 3-D structures, the surface-to-volume ratio increases as the size increases,[29] and more atoms inaccessible to the reaction would appear. These inner atoms would lower the APUM of a given sub-nano-Au cluster. More *Face* sites among surface sites participate in the reaction. Although there are an increasing number of *Face* sites in larger Au clusters, it can be clearly seen from Fig. 7(c) that the catalytic performance of *Face* sites is significantly weaker than that of other types of sites, which also results in the catalytic activity of sub-nano-Au clusters decreasing with the increase of cluster size.

In Fig. 7(d), the contribution of different surface sites is illustrated, respectively. It is obvious that *Kink* sites dominate the catalytic reaction at a very small size of Au clusters. When $N > 50$, more and more *Face* sites start to participate in the contribution of the whole cluster catalysis. Although *Face* sites show inferior catalytic performance in Fig. 7(c), the increasing number of *Face* atoms in relatively large clusters remarkably compensates for their poor individual ability. From 50 to 150 atoms, the APUM decreases with increasing cluster size due to the higher and higher contributors to the overall cluster catalytic rate from *Face* sites. After 150 atoms, although the contribution distribution and average rate of surface sites remain largely unchanged (Fig. 7d and Fig. S10†), the decreasing surface site percentage becomes the main reason for the reduction in the APUM. Meanwhile, the decreasing contribution of *Kink* sites with increasing cluster size does not mean that *Kink* sites are catalytically inactive. This phenomenon is attributed to the small number of *Kink* sites in large clusters because the shape of clusters becomes more regular when the size increases. Tatsuya *et al.*[51] studied the aerobic oxidation of size-controlled Au clusters smaller than 2 nm, and they selected Au_N ($N = 10, 18, 25, 39,$ and 85) and fitted the TOF curve based on these 5 data points. Their experimental data have something in common with our computational results; the activity curve in their work decreases when N exceeds 50. A similar phenomenon also appears in Fig. 7(a), where Au clusters consisting of fewer than 50 atoms show better catalytic activity.

3.5 CO oxidation kinetics controlled by site-dependent adsorption on sub-nano-Au clusters

As the cluster size increases, the reaction phenomenon yields a paradox that despite the decreasing energy barrier in Fig. 5(d), the overall catalytic performance of clusters in Fig. 7 (a and b) still deteriorates. The adsorption energy of all types of reaction sites is discussed in Fig. 8(a and b). For both CO and O_2 adsorption, the *Face* sites show significantly weaker adsorption than other types of sites. In the adsorption of molecular oxygen, *Face* sites tend to produce positive adsorption energy, which is also consistent with the previous description that O_2 cannot adsorb on these highly coordinated atoms. Due to the inability of these *Face* sites to adsorb the reactants efficiently, this leads to the poor catalytic performance of the *Face* sites to some extent. Although the reduction of the rate-controlled energy barrier makes the reaction easier to proceed,
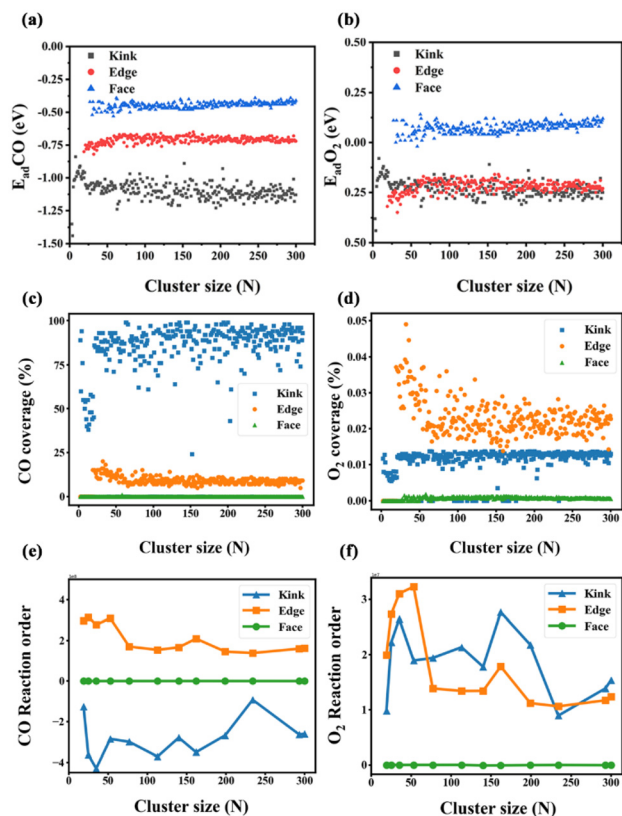
Fig. 8 (a) The distribution of CO adsorption energy on different surface sites (*Kink*, *Edge*, and *Face*) of sub-nano-Au clusters as a function of the number of Au atoms. (b) The distribution of O_2 adsorption energy on different surface sites of sub-nano-Au clusters as a function of the number of Au atoms. (c) The coverage of CO on different surface sites of sub-nano-Au clusters as a function of the number of Au atoms. (d) The coverage of O_2 on different surface sites of sub-nano-Au clusters as a function of the number of Au atoms. (e) The CO reaction order on different surface sites of sub-nano-Au clusters as a function of the number of Au atoms. (f) The O_2 reaction order on different surface sites of sub-nano-Au clusters as a function of the number of Au atoms.

too weak adsorption of the reactants still makes it difficult to even start the reaction. Fig. 7(c and d) discuss the coverage of CO and O_2 on the cluster surface. CO molecules show a high coverage at *Kink* sites, while showing a medium coverage at *Edge* sites. However, the coverage of CO on these two types of sites is far higher than that on *Face* sites, rationalizing the weak adsorption of *Face* sites leading to a low reaction rate. Compared with the CO coverage, the O_2 coverage at the *Face* sites is significantly weaker by several orders of magnitude, which indicates that the adhesion of O_2 at the *Face* sites of clusters is more difficult.[50] Given the fact that the O_2 coverage is extremely low, the coverage of the *Face* sites is still the lowest compared with other types of sites, which further explains the poor reaction performance of *Face* sites. Both *Edge* sites and *Kink* sites exhibit disparities in their CO coverage and O_2 coverage, with *Kink* sites demonstrating much higher CO coverage characteristics but a much lower O_2 coverage compared to *Edge* sites. David M. Rayner's group explored CO adsorption on

Au clusters aided by infrared photodepletion spectroscopy to record the vibrational spectra of Au–CO complexes. Additionally, they use infrared reflectance measurements to find that low-coordinated Au atoms (*Kink* and *Edge* sites) tend to adsorb CO molecules at a low CO coverage because of their strong CO binding. CO binds preferentially to Au atoms in low coordination, whereas highly coordinated Au atoms (*Face* sites) are not reactive toward CO.[52] Whetten's group studied molecular oxygen adsorption[53–55] over Au clusters and established a binary-like adsorption behaviour (either zero or one O_2 adsorbed), which could rationalize the simulated weak adsorption and low coverage of O_2.

The reaction orders determined by varying the partial pressures of CO and O_2 respectively are shown in Fig. 8(e and f). So as to explore the size-dependent reaction order, some clusters are randomly selected with atom number as 19, 25, 35, 53, 77, 113, 140, 162, 199, 234, 293, and 300. The reaction order of *Face* sites remains zero no matter how the size of the cluster changes, which indicates that the variation of neither CO partial pressure nor O_2 partial pressure has any effect on the activity of *Face* sites. In other words, *Face* sites are very insensitive to the external atmosphere, which indicates that these gas molecules have very weak adsorption at *Face* sites. In Fig. 8(e), *Kink* sites show negative reaction orders when changing the amount of CO, which could be attributed to extremely strong CO adsorption and excessively high CO coverage at *Kink* sites. Because of these reasons, when a continuous increase in the partial pressure of CO happens, *Kink* sites are poisoned and their reaction processing is hindered, and such similar results have also been reported in the previous work.[43–45,49] The reaction order of *Kink* sites adsorbing O_2 and all *Edge* sites is always positive when the size changes. In contrast to *Face* sites, the increase of the corresponding gas partial pressure promotes the reaction on these types of sites. This phenomenon can be attributed to the fact that the adsorption at *Edge* sites and the adsorption of O_2 at *Kink* sites are far from reaching their saturation state. Therefore, increasing the corresponding partial pressure of CO or O_2 will promote the adsorption of their respective reactants and thus play a positive role in boosting the CO oxidation reaction rate.

Based on the above discussions, the results of the rate-mapping color model in Fig. 6 could be interpreted reasonably. Observing the distribution of active sites in clusters of different sizes, it can be concluded that the *Face* site activity of large clusters is very low, while the *Face* site activity of small clusters is generally high but the *Kink* site activity is poor. These intuitive results conform well to the geometric features of surface sites, and only suitable adsorption and coverage facilitate an easy CO oxidation process. In small clusters such as Au_6 and Au_{19}, *Kink* sites exhibit too strong CO adsorption, which hinders the corresponding activity. Larger clusters such as Au_{293} and Au_{300} tend to possess surfaces consisting of *Face* sites, which generate a low coverage of the reactant and make it difficult to adsorb the reactant. In contrast, the *Edge* sites exhibit moderate adsorption strength and reactant coverage, which leads to their generally better catalytic performance.

4 Conclusions

In this paper, a systematic study of Au_N (N = 2–300) sub-nano-clusters for CO oxidation is conducted, focusing on the size effect on their adsorption and catalytic activity. The RPSO method is used to screen out the globally optimal structure of the chosen sub-nano-Au clusters. Geometric descriptors, including CN_g and CA_r, are used to describe the geometric features of reaction sites, which help to build the geometric–adsorption–activity correlation and enable the evaluation of the reaction rate of each site for any given sub-nano-Au cluster. The distinctive catalytic performance of different geometric structural sites has also been discussed to rationalize the volcano-shaped relationship of size-dependent activity per unit mass. This volcano-shaped reactivity conforms well with the experimental result of Tatsuya's work.[51] Due to the different local atom arrangements at the reaction sites of sub-nano-Au clusters of different sizes, the adsorption of CO and O_2, the energy barrier of the surface elementary reaction, and the site contribution to the overall reaction all exhibit significant size effects. The interplay of these factors has resulted in the outcome that around Au_{25} (or 0.75 nm) is located at the volcano peak. Moreover, while similar adsorption behaviors have been observed in experiments, mostly focusing on limited sizes (<100), our work makes reasonable predictions for larger-scale adsorption.[52–55] This study further explores the research paradigm of catalytic mechanisms at the site level, contributing to a fundamental understanding of size-dependent activity over sub-nano-Au catalysts. In the future, this type of precise site-level reaction simulation may further promote the development of catalytic science and boost the research progress of high-performance sub-nano-catalysts' rational design.

Data availability

The data supporting this article have been included as part of the ESI.† The structure data for Au_N (2–300) as *XYZ* files have been deposited at **https://doi.org/10.1039/d4nr02705a**.

Conflicts of interest

There are no conflicts to declare.

Acknowledgements

References

1 G. J. Hutchings, *J. Catal.*, 1985, **96**, 292–295.

2 B. G. Donoeva, D. S. Ovoshchnikov and V. B. Golovko, *ACS Catal.*, 2013, **3**, 2986–2991.

3 M. Valden, X. Lai and D. W. Goodman, *Science*, 1998, **281**, 1647–1650.

4 G. Li and R. Jin, *Acc. Chem. Res.*, 2013, **46**, 1749–1758.

5 S. Yamazoe, K. Koyasu and T. Tsukuda, *Acc. Chem. Res.*, 2014, **47**, 816–824.

6 S. K. Shaikhutdinov, R. Meyer, M. Naschitzki, M. Bäumer and H.-J. Freund, *Catal. Lett.*, 2003, **86**, 211–219.

7 G. R. Bamwenda, S. Tsubota, T. Nakamura and M. Haruta, *Catal. Lett.*, 1997, **44**, 83–87.

8 C. Lemire, R. Meyer, S. Shaikhutdinov and H. Freund, *Angew. Chem., Int. Ed.*, 2004, **43**, 118–121.

9 G. Li, D. Jiang, S. Kumar, Y. Chen and R. Jin, *ACS Catal.*, 2014, **4**, 2463–2469.

10 M. M. Kappes, P. Radi, M. Schär and E. Schumacher, *Chem. Phys. Lett.*, 1985, **119**, 11–16.

11 M. M. Kappes, R. W. Kunz and E. Schumacher, *Chem. Phys. Lett.*, 1982, **91**, 413–418.

12 Y. Zhang, P. Song, T. Chen, X. Liu, T. Chen, Z. Wu, Y. Wang, J. Xie and W. Xu, *Proc. Natl. Acad. Sci. U. S. A.*, 2018, **115**, 10588–10593.

13 N. Lopez and J. K. Nørskov, *J. Am. Chem. Soc.*, 2002, **124**, 11262–11263.

14 D. M. Popolan and T. M. Bernhardt, *J. Chem. Phys.*, 2011, **134**, 091102.

15 L. D. Socaciu, J. Hagen, T. M. Bernhardt, L. Wöste, U. Heiz, H. Häkkinen and U. Landman, *J. Am. Chem. Soc.*, 2003, **125**, 10437–10445.

16 F. H. Kaatz, D. Yu. Murzin and A. Bultheel, *ACS Catal.*, 2021, **11**, 9073–9085.

17 Y. Zhou, Z. Zhao and D. Cheng, *Comput. Phys. Commun.*, 2020, **247**, 106945.

18 Z. Deng, Y. Zhou, L. Zhao and D. Cheng, *Mol. Simul.*, 2022, **48**, 891–901.

19 D. J. Wales and J. P. K. Doye, *J. Phys. Chem. A*, 1997, **101**, 5111–5116.

20 CEC-Benchmark-Functions/CEC2017/CEC-Benchmark-Functions, **https://github.com/tsingke/CEC-Benchmark-Functions/tree/master/CEC2017**.

21 F. Cleri and V. Rosato, *Phys. Rev. B: Condens. Matter Mater. Phys.*, 1993, **48**, 22–33.

22 Y. Pei and X. C. Zeng, *Nanoscale*, 2012, **4**, 4054.

23 B. Assadollahzadeh and P. Schwerdtfeger, *J. Chem. Phys.*, 2009, **131**, 064306.

24 G. Kresse and J. Furthmüller, *Comput. Mater. Sci.*, 1996, **6**, 15–50.

25 alphashape·PyPI, **https://pypi.org/project/alphashape/**.

26 B. Yoon, H. Häkkinen, U. Landman, A. S. Wörz, J.-M. Antonietti, S. Abbet, K. Judai and U. Heiz, *Science*, 2005, **307**, 403–407.

27 H. Xu, D. Cheng, Y. Gao and X. C. Zeng, *ACS Catal.*, 2018, **8**, 9702–9710.

28 H. Li, L. Li, A. Pedersen, Y. Gao, N. Khetrapal, H. Jonsson and X. C. Zeng, *Nano Lett.*, 2015, **15**, 682–688.

29 O. D. Häberlen, S.-C. Chung, M. Stener and N. Rösch, *J. Chem. Phys.*, 1997, **106**, 5189–5201.

30 L. Xiao, B. Tollberg, X. Hu and L. Wang, *J. Chem. Phys.*, 2006, **124**, 114309.

31 A. Sebetci and Z. B. Güvenç, *Modell. Simul. Mater. Sci. Eng.*, 2005, **13**, 683–698.

32 S. Heiles, A. J. Logsdail, R. Schäfer and R. L. Johnston, *Nanoscale*, 2012, **4**, 1109–1115.

33 J. Wang, G. Wang and J. Zhao, *Phys. Rev. B: Condens. Matter Mater. Phys.*, 2002, **66**, 035418.

34 X.-B. Li, H.-Y. Wang, X.-D. Yang, Z.-H. Zhu and Y.-J. Tang, *J. Chem. Phys.*, 2007, **126**, 084505.

35 F. Calle-Vallejo, J. I. Martínez, J. M. García-Lastra, P. Sautet and D. Loffreda, *Angew. Chem., Int. Ed.*, 2014, **53**, 8316–8319.

36 F. Calle-Vallejo, J. Tymoczko, V. Colic, Q. H. Vu, M. D. Pohl, K. Morgenstern, D. Loffreda, P. Sautet, W. Schuhmann and A. S. Bandarenka, *Science*, 2015, **350**, 185–189.

37 X. Kuang, X. Wang and G. Liu, *Phys. E*, 2012, **44**, 2132–2137.

38 J. L. C. Fajín, M. N. D. S. Cordeiro and J. R. B. Gomes, *J. Phys. Chem. C*, 2008, **112**, 17291–17302.

39 C.-C. Lee and H.-T. Chen, *J. Phys. Chem.*, 2015, **119**, 8547–8555.

40 B. Yoon, H. Häkkinen and U. Landman, *J. Phys. Chem. A*, 2003, **107**, 4066–4071.

41 M. A. Dar and S. Krishnamurty, *ACS Omega*, 2019, **4**, 12687–12695.

42 A. Hussain, D. Curulla Ferré, J. Gracia, B. E. Nieuwenhuys and J. W. Niemantsverdriet, *Surf. Sci.*, 2009, **603**, 2734–2741.

43 F. Mehmood, A. Kara, T. S. Rahman and C. R. Henry, *Phys. Rev. B: Condens. Matter Mater. Phys.*, 2009, **79**, 075422.

44 B. Hammer, Y. Morikawa and J. K. Nørskov, *Phys. Rev. Lett.*, 1996, **76**, 2141–2144.

45 A. J. Medford, J. Wellendorff, A. Vojvodic, F. Studt, F. Abild-Pedersen, K. W. Jacobsen, T. Bligaard and J. K. Nørskov, *Science*, 2014, **345**, 197–200.

46 C. R. Harris, K. J. Millman, S. J. Van Der Walt, R. Gommers, P. Virtanen, D. Cournapeau, E. Wieser, J. Taylor, S. Berg, N. J. Smith, R. Kern, M. Picus, S. Hoyer, M. H. Van Kerkwijk, M. Brett, A. Haldane, J. F. Del Río, M. Wiebe, P. Peterson, P. Gérard-Marchant, K. Sheppard, T. Reddy, W. Weckesser, H. Abbasi, C. Gohlke and T. E. Oliphant, *Nature*, 2020, **585**, 357–362.

47 B. Hammer and J. K. Norskov, *Nature*, 1995, **376**, 238–240.

48 A. Ruban, B. Hammer, P. Stoltze, H. L. Skriver and J. K. Nørskov, *J. Mol. Catal. A: Chem.*, 1997, **115**, 421–429.

49 A. A. Koverga, S. Frank and M. T. M. Koper, *Electrochim. Acta*, 2013, **101**, 244–253.

50 J. Kleis, J. P. Greeley, N. A. Romero, V. A. Morozov, H. Falsig, A. H. Larsen, J. Lu, J. J. Mortensen, M. Dułak, K. S. Thygesen, J. K. Nørskov and K. W. Jacobsen, *Catal. Lett.*, 2011, **141**, 1067–1071.

51 Y. Liu, H. Tsunoyama, T. Akita, S. Xie and T. Tsukuda, *ACS Catal.*, 2011, **1**, 2–6.

52 A. Fielicke, G. Von Helden, G. Meijer, D. B. Pedersen, B. Simard and D. M. Rayner, *J. Am. Chem. Soc.*, 2005, **127**, 8416–8423.

53 B. E. Salisbury, W. T. Wallace and R. L. Whetten, *Chem. Phys.*, 2000, **262**, 131–141.

54 W. T. Wallace and R. L. Whetten, *J. Phys. Chem. B*, 2000, **104**, 10964–10968.

55 W. T. Wallace and R. L. Whetten, *J. Am. Chem. Soc.*, 2002, **124**, 7499–7505.